Afternoon precipitation peak simulated in an aqua-planet global non-hydrostatic model (aqua-planet-NICAM)

By

Kazuaki YASUNAGA*1, Tomoe NASUNO*2, Hiroaki MIURA*2,

Yukari N. TAKAYABU*1, and Masanori YOSHIZAKI*1

***1** *Institute of Observational Research for Global Change, Japan Agency for Marine-Earth Science and Technology (IORGC, JAMSTEC), Yokosuka, Japan*

***2** *Frontier Research Center for Global Change, Japan Agency for Marine-Earth Science and Technology (FRCGC, JAMSTEC), Yokohama, Japan*

Submitted to JMSJ

February 2009

Corresponding Author's Address:

Dr. Kazuaki Yasunaga, Institute of Observational Research for Global Change, Japan Agency for Marine-Earth Science and Technology (IORGC, JAMSTEC), Yokosuka, Kanagawa, 237-0061, Japan;

E-mail: yasunaga@jamstec.go.jp, Phone: +81-46-867-9851, Fax:+81-46-867-9255

Abstract

An aqua-planet simulation using the Nonhydrostatic ICosahedral Atmospheric Model (NICAM) shows a diurnal precipitation cycle with a minor maximum in the afternoon, even though sea-surface temperature is constant during the integration. The present study explores the factors that control the afternoon precipitation peak, making use of the simulation results.

The temperature in the lower troposphere shows a minor minimum in the afternoon, coinciding with the precipitation peak. It is suggested that the "squeezing through temperature reduction" (whereby condensation is enhanced and more water vapor is squeezed within a cloud due to reduced temperature) is the most important factor in explaining the afternoon precipitation peak. The temperature minimum is associated with a dynamical process (not a diabatic process), and its relationship with the atmospheric tide is discussed.

1. Introduction

Global circulation is strongly affected by tropical convective activity via the latent heat released by convection. Temporal variations in tropical convection occur at various scales ranging from half a day to 30–60 days. The diurnal cycle, resulting from radiative forcing by the sun, is one of the most fundamental cycles; consequently, it has been the subject of many previous studies.

Diurnal variations in rainfall over tropical oceanic regions free from continental influence show various features depending on the nature of large-scale convective activity. During the convectively active period, the diurnal cycle in rainfall shows a peak in the early morning. During the convectively suppressed period, in contrast, peaks in rainfall occur during the afternoon and early morning. The diurnal variation in sea-surface temperature (SST) is pronounced during the convectively suppressed (undisturbed) period (e.g., Johnson et al. 1999), and the atmospheric mixed layer over the ocean behaves like that over land. Accordingly, skin SST diurnal variations have been attributed to the afternoon maximum in rainfall (e.g., Chen and Houze 1997; Sui et al. 1997; Johnson et al. 2001). Making use of observational data obtained over the tropical Indian Ocean, Yasunaga et al. (2008) noted that the daytime increase in precipitable water and rainfall correspond to the large SST increase during the undisturbed period; however, the surface fluxes cannot completely account for the observed increase in precipitable water, and the importance of SST in terms of the afternoon precipitation peak remains a matter of controversy.

Non-hydrostatic models, which can adequately represent clouds, are a powerful and convenient tool in examining the development of cumulus convection, and have been used in many previous studies to investigate diurnal variations in rainfall (e.g., Liu and Moncrieff 1998; Sui et al. 1998; Kubota et al. 2004). Tomita and Satoh (2004) developed the Nonhydrostatic ICosahedral Atmospheric Model (NICAM), and Tomita et al. (2005) reported the results of global non-hydrostatic simulations for an aqua-planet condition with a horizontal mesh size down to 3.5 km.

Aqua-planet NICAMs with a horizontal grid spacing of 7 and 3.5 km (hereafter referred to as Exp-7km and Exp-3.5km, respectively) simulate a diurnal precipitation cycle with a minor maximum in the afternoon (1200–1500 local time (LT)), as well as a predawn peak (0300–0600 LT) (Fig. 1). SST is constant during the integration, raising the possibility that factors other than SST variations play a role in generating the simulated afternoon rainfall maximum.

The present study explores the factors that control the development of the afternoon precipitation peak, making use of simulation data produced by Exp-7km and Exp-3.5km. Even a horizontal grid spacing of 3.5 km is insufficient to represent shallow cumulus, and the timing of the development of deep convection is possibly influenced by the coarse horizontal grid spacing of the model. Therefore, Exp-7km and Exp-3.5km cannot be referred as a cloud-resolving model simulation. Despite these potential limitations, it is the first attempt to simulate atmospheric general circulation using a three-dimensional non-hydrostatic model with a grid spacing of a few kilometers. Such a global simulation involves the fewest uncertainties among the various models currently available. In this context, it is useful to describe the afternoon peak in precipitation reproduced by the aqua-planet NICAM. Moreover, the simple framework of the aqua-planet condition (with a constant SST) will prove beneficial in seeking to understand the observed afternoon rainfall peak.

The remainder of the paper is organized as follows. The experimental design for the current series of simulations is the same as that employed in Tomita et al. (2005) and Nasuno et al. (2007); however, for the reader's convenience the numerical model and experimental setup are briefly described in Section 2. Various aspects of the afternoon rainfall peak are presented in Section 3, and the process responsible for the afternoon peak is described in Section 4. Section 5 considers daytime variations in temperature, and the main conclusions are summarized in Section 6.

2. Model and experimental setup

The model used in the present study is NICAM, as developed at the Frontier Research Center for Global Change (FRCGC), Japan. The model equations are based on a nonhydrostatic framework (Tomita and Satoh 2004), and guarantee the conservation of total mass and total energy (Satoh et al. 2008). The employed conservation property is suitable for long-term simulations.

The horizontal grid interval in the experiment analyzed in the present investigation is 7 km. The model has 54 levels in the vertical (model top at 40 km), with a fine grid spacing (75 m) within the lowest level and a relatively coarse grid spacing (750 m) in the upper levels. The time interval is 30 sec. Moist processes are represented using the simple cloud-microphysics scheme proposed by Grabowski (1998); no cumulus parameterization is employed. The level-2 closure model (Mellor and Yamada 1974) is applied to represent turbulent diffusion. The radiation and surface flux schemes are based on those proposed by Nakajima et al. (2000) and Louis (1979), respectively. Solar radiation is assumed to be above the equator (equinox), and radiation is calculated every 10 min; other physical processes are updated at each time step.

SST is fixed at a zonally uniform value with a peak at the equator, and the aqua-planet setup is based on the method proposed by Neale and Hoskins (2000). Making use of the results obtained from a 3.5-year integration with a conventional AGCM with T42L59 resolution, the simulation with a 14-km horizontal grid spacing is integrated for 90 days. The results on the 60th day are interpolated, and a 30-day integration is performed with a grid spacing of 7 km. In turn, the Exp-7km results on the 20th day are utilized as the initial conditions for a 10-day integration for Exp-3.5km. In the simulations with the finer grid spacing, nudging technique is not used. The limitations of available computing resources mean that only two-dimensional data are available in the Exp-3.5km with a temporal resolution of 1.5 hours (values are averages for each 1.5-hour period; 0000-0130Z, 0130-0300Z, …), while two- and three-dimensional data are available for Exp-7km with a temporal interval of 3 hours (values are averages for each 3-hour period; 0000-0300Z, 0300-0600Z, …).

3. Diurnal variation in precipitation

Precipitation amounts are concentrated around the equator (about 70 % within 3°S–3°N), since SST is the highest at the equator (See Tomita et al. 2005). The most notable feature in rainfall diurnal variations is that a more realistic diurnal cycle with a major peak in the early morning is simulated in the NICAM than in a conventional AGCM with T42L59 resolution which uses the Arakawa-Schubert cumulus parameterization (The latter simulates precipitation peak at midnight), as described in Tomita et al. (2005).

The afternoon peak is only found close to the equator, whereas the predawn peak is dominant at all latitudes; the poleward phase shift is not recognized (not shown). Therefore, the mean over the equator region (within 3°S–3°N) is discussed afterwards.

Figure 2 shows a longitude–time (UTC) cross-section of precipitation anomalies. The precipitation anomaly has a zonal wavenumber of 2, and migrates westward around the earth over the course of a day, indicating that the afternoon peak does not depend on a local event at a specific longitude. Moreover, the semi-diurnal harmonic, which largely contributes to the afternoon peak, has a min-to-max range comparable to the diurnal harmonic especially in the Exp-3.5km (Solid and dashed lines in Fig. 1). Namely, it can be considered that the afternoon peak would be neither insignificant nor accidental, although the afternoon peak is weaker than the predawn peak. Large contribution of semi-diurnal harmonic is also found in other aqua-planet AGCM simulation (Woolnough et al. 2004) and is not special in the simulations by NICAM.

The simulated diurnal variations in column-integrated cloud and rain water show more prominent afternoon peaks (Figs. 3a and 3c) than those in precipitation (Fig. 2). The semi-diurnal harmonic has a min-to-max range comparable to the diurnal harmonic especially in the Exp-3.5km (not shown). In contrast, variations in column-integrated cloud ice and have no (or slight) afternoon peak (Figs. 3b and 3d), and little contribution of the semi-diurnal harmonics is found (not shown). Therefore, the afternoon peak would be mainly related to warm rain processes in the lower troposphere. These features are discussed in the section 4.4.

4. What factors are responsible for the afternoon precipitation peak?

In the absence of any change in SST, four factors have the potential to influence precipitation: (1) moisture increase, (2) horizontal convergence, (3) conditional instability, and (4) the “squeezing through temperature reduction” of water vapor. The following sections examine in detail whether each of these factors might play a critical role in controlling the simulated afternoon precipitation peak. Sui et al. (1998) pointed out that rainfall maximum in the predawn is related to time variations of the vertically integrated saturation water vapor amount. The 4th mechanism (squeezing of water vapor through temperature reduction) is essentially identical to that proposed by Sui et al. (1998), and the basic idea is also described in the section 4.4.

4.1. Moisture increase

Figure 4 shows diurnal variations in precipitable water. A diurnal cycle is dominant, with a minimum in the predawn period and maximum in the evening—the opposite trend to that observed for precipitation. There is no precipitable water maximum associated with the afternoon rainfall peak; therefore, variations in atmospheric moisture would be of secondary importance in terms of explaining the afternoon precipitation peak.

4.2. Horizontal convergence

Figure 5 shows diurnal variations in horizontal wind divergence. A clear diurnal cycle is simulated, with convergence in the lower troposphere showing a peak at 0600–0900 LT; there is no convergence maximum associated with the afternoon precipitation peak. Moreover, vertically integrated mass convergence (below 12km) exhibits the peak at 1500-1800 LT (not shown), which follows the afternoon precipitation peak (1200-1500 LT). Therefore, horizontal wind convergence cannot account for the afternoon precipitation peak, although horizontal convergence possibly contributes to the predawn peak.

4.3. Conditional instability

To examine the environmental conditions necessary for convective development, we calculated the convective available potential energy (CAPE) and convective inhibition (CIN) using temperature and water-vapor profiles averaged over the region 3°S–3°N for a period of 30 days. In the calculation, air is assumed to be well mixed below a height of 450 m, and air with the mean values of potential temperature and mixing ratio for 0–450 m height is raised from the surface to the level of neutral buoyancy (LNB) through the level of free convection (LFC).

CAPE shows a peak around midnight (Fig. 6a), while CIN attains a minimum during the predawn period (Fig. 7b). Although temperature near the surface is low around the predawn and early morning period (Fig. 7c), the height of LFC is also lowered, resulting in the CIN minimum. The CAPE maxima and CIN minimum precede or are synchronous with the predawn peaks in precipitation, which is possibly influenced by variations in CAPE and CIN, as there is a lag in the response of convection to changes in environmental conditions; however, no CAPE maxima or CIN minima correspond to the minor afternoon precipitation peak. Accordingly, the variations in CAPE and CIN are unable to account for the afternoon precipitation peak.

4.4. Squeezing of water vapor through temperature reduction

When temperature decreases dynamically in an atmospheric column, condensation is enhanced due to the lowered saturation vapor pressure. A relatively large amount of water vapor is squeezed within a cloud (or the area with high-relative humidity) with a lowering of temperature, resulting in greater precipitation. The mechanism of “squeezing through temperature reduction” considered here is essentially identical to that proposed by Sui et al. (1998).

First, the squeezing mechanism is qualitatively evaluated. Variations in temperature at 2 m show a minor minimum at 1200–1500 LT (Fig. 7), coinciding with the rainfall peak. Two-meter temperature minima are recognized only near the equator (data not shown), in agreement with the region of the afternoon rainfall peak. The temperature minimum at 0300–0600 LT extends throughout the entire troposphere, whereas that at 1200–1500 LT is limited to the lower and middle troposphere (Fig. 8a). The temperature variations in the lower and middle troposphere are largely contributed to by the semidiurnal component and afternoon minimum is found in the total temperature variations, although the diurnal component almost entirely dominates temperature variation in the upper troposphere (Figs. 8b and 8c). Variations in liquid water, which forms in the lower troposphere, show an afternoon peak, whereas solid water, which forms in the upper troposphere, shows no such peak (Fig. 3). These results are consistent with the operation of the squeezing mechanism.

Variations in the number of precipitating grids show minor and no afternoon peaks in the Exp-3.5km and Exp-7km, respectively (Figs. 9a and 9c). In contrast, much clearer afternoon peaks are found in variations of precipitation rate averaged over precipitating grids (Figs. 9b and 9d). “Squeezing through temperature reduction" works only around the saturation condition, because the temperature reduction is small. Therefore, it can enhance condensation within existing clouds, but cannot effectively promote the formation of new clouds. Considering these characteristics, the results shown in Fig. 9 further support the proposal that ”squeezing through temperature reduction” is a dominant control on the simulated afternoon rainfall peak.

Next, the mechanism of squeezing through temperature reduction is quantitatively evaluated. It is assumed that the atmosphere can retain 75% of the saturated precipitable water (herein termed the temperature-derived precipitable water; TPW). This assumption is based on the fact that precipitable water averaged over the region 3°S–3°N over 30 days (49.225 mm) is comparable to the TPW calculated under the above assumption (49.669 mm). The calculated TPWs for the periods 0900–1200, 1200–1500, and 1500–1800 LT are 49.724, 49.669, and 49.729 mm, respectively, with the differences between the successive TPWs being -0.055 and +0.060 mm. If we consider that the difference represents squeezed water vapor due to reduced temperature and that the variation occurs over a period of 3 hours, the difference between the precipitation rates calculated for the periods 0900–1200 and 1200–1500 LT is +0.018 mm hr^{-1}. The difference between the simulated rainfall rates for 0900–1200 LT (1.0471 mm hr^{-1}) and 1200–1500 LT (1.0633 mm hr^{-1}) is about +0.0162 mm hr^{-1} (see Fig. 1). Similarly, the difference between the precipitation rates calculated for 1200–1500 and 1500–1800 LT is -0.02 mm hr^{-1}, and the difference in the simulated rainfall rate for 1200–1500 and 1200–1500 LT (1.0422 mm hr^{-1}) is about -0.0221 mm hr^{-1}. These rough estimates are sufficient in quantitatively accounting for the minor afternoon peak, although the temperature difference is quite small.

The minima of PW and temperature anomaly in the local afternoon migrates westward around the earth over the course of a day (Figs. 10 and 11) together with the precipitation anomaly (Fig. 2), and almost coincides with the precipitation peak. These results further support the "squeezing through temperature reduction". On the other hand, it is not clear that the temperature minimum is independent to the evaporation cooling of rain drops. Therefore, the following section discusses the factor that controls the afternoon temperature minimum.

5. Discussions: Conceivable factors controlling the afternoon temperature minimum

Variation in sensible heat flux shows peaks at 0300–0600 and 1200–1500 LT, and is 180° out of phase with variations in temperature at 2 m (data not shown). Variations in temperature at 2 m over non-precipitating grids show similar patterns to those over all grids within 3°S–3°N (circles in Fig. 7); furthermore, diabatic heating variations in the lower troposphere also peak at 1200–1500 LT (Fig. 12). These results indicate that the afternoon temperature minimum does not result from the surface flux or evaporation of condensates. Moreover, radiative forcing shows a clear diurnal cycle: radiative heating peaks at 1200–1500 LT, while near-constant radiative cooling is found from 1800 to 0600 LT (data not shown). Therefore, radiative forcing cannot account for the temperature minimum at 1200–1500 LT, and it can be considered that the temperature minimum near the equator is associated with a dynamical process rather than a diabatic process.

As described in the previous section, the simulated temperature anomaly at 2 m has a zonal wavenumber of 2, and migrates westward around the earth over the course of a day (Fig. 10). The timing of the temperature minimum (and precipitation peak) coincides with that of the pressure minimum. Surface pressure (Ps) shows a clear semidiurnal cycle with a min-to-max range of about 1.2 hPa in the Exp-3.5km, with minima peaks at 0300–0600 and 1500–1800 LT and maxima at 0900–1200 and 2100–2400 LT. The Ps amplitude and peak time are roughly in agreement with those associated with the semidiurnal component of the atmospheric tide (e.g., Dai and Wang 1999), and the dynamical response to radiation heating is responsible for the Ps variations. Based on the temporal coincidence with Ps variations, the afternoon temperature minimum is considered to be associated with the semidiurnal component of the atmospheric tide; however, the top of the model domain at 40 km is set in the middle of the region of peak ozone forcing, which is considered a major forcing for the semidiurnal tide. It is therefore possible that the artificial boundary condition has a strong influence on the behavior of the atmospheric tide. However, global scale wave model (GSWM; Hagan et al. 1995), which is developed to examine the thermally-driven response for diurnal and semidiurnal atmospheric tides, and an aquaplanet AGCM which has enough vertical domain (Woolnough et al. 2004) also show the surface temperature minimum around 1200-1500LT. Therefore, the afternoon temperature minimum in the present experiment is not completely artificial, and would be the atmospheric dynamical response for the solar heating.

6. Summary

Recent advances in computational resources have enabled us to conduct global non-hydrostatic simulations with a horizontal grid spacing of several kilometers. Using the Nonhydrostatic ICosahedral Atmospheric Model (NICAM) developed by Tomita and Satoh (2004), Tomita et al. (2005) conducted global non-hydrostatic simulations for an aqua-planet condition with a horizontal mesh size down to 3.5

km, and reported a diurnal precipitation cycle with a minor maximum in the afternoon (1200–1500 LT) and a predawn peak (0300–0600 LT), even though SST remained constant during the integration. The present study explored the factors that control the afternoon precipitation peak, making use of simulation data produced by the aqua-planet NICAM with a horizontal grid spacing of 3.5km and 7 km.

The afternoon rainfall peak is only found close to the equator, and migrates westward around the earth over the course of a day with a zonal wavenumber of 2. Variations in column-integrated cloud and rain water also show the afternoon peak, whereas variations in column-integrated cloud ice and snow only show a predawn peak.

In the absence of any change in SST, there exist four candidate processes in terms of controlling the afternoon precipitation peak: (1) moisture increase, (2) horizontal convergence, (3) conditional instability, and (4) the squeezing of water vapor through temperature reduction. There exist no peaks in precipitable water, horizontal wind convergence, CAPE, or CIN associated with the afternoon rainfall peak, and the peak cannot be explained by variations in atmospheric moisture, horizontal wind convergence, CAPE, or CIN. In contrast, variations in temperature in the lower troposphere show a minor minimum in the afternoon, coinciding with the precipitation peak. Condensation is enhanced and more water vapor is squeezed within a cloud due to the reduction in temperature that results in a lowering in saturation vapor pressure. The results of qualitative and quantitative analysis indicate that "squeezing through temperature reduction" is the dominant control on the simulated afternoon rainfall peak. The importance of the squeezing mechanism has been reported by Sui et al. (1998), although only radiative cooling during nighttime was considered. A new factor identified in the present study is temperature decrease during the daytime.

The temperature minimum is limited to areas near the equator (within 6°S–6°N) and is associated with a dynamical process (not a diabatic process such as sensible heat flux, evaporation of condensates, or radiation). The simulated temperature anomaly near the surface migrates westward around the earth over the course of a day with a zonal wavenumber of 2. The timing of the temperature minimum (and precipitation peak) coincides with that of the pressure minimum, and it is suggested that the semidiurnal component of the atmospheric tide is responsible for the afternoon temperature minimum. Further investigations are needed to clarify the relationship between temperature variations and the atmospheric tide.

Acknowledgments

Calculations for this study took place at Earth Simulator in the Earth Simulator Center of the Japan Agency for Marine-Earth Science and Technology. Comments by Dr. Nakajima and two anonymous reviewers lead to improvements in the present manuscript. All of the figures were drawn using GrADS software (URL: http://www.iges.org/grads/).

Reference

Chen, S. S. and R. A. HouzeJr., 1997: Diurnal variation and life-cycle of deep convective systems over the tropical pacific warm pool. Quart. J. Roy. Meteor. Soc., 123, 357-388.

Dai, A. and J. Wang, 1999: Diurnal and Semidiurnal Tides in Global Surface Pressure Fields. J. Atmos. Sci., 56, 3874-3891.

Grabowski, W. W., 1998: Toward Cloud Resolving Modeling of Large-Scale Tropical Circulations: A Simple Cloud Microphysics Parameterization. J. Atmos. Sci., 55, 3283-3298.

Hagan, M., J. Forbes, and F. Vial, 1995: On Modeling Migrating Solar Tides, Geophys. Res. Lett., 22(8), 893-896.

Johnson, R. H., T. M. Rickenbach, S. A. Rutledge, P. E. Ciesielski, and W. H. Schubert, 1999: Trimodal Characteristics of Tropical Convection. J. Clim., 12, 2397-2418.

Johnson, R. H., P. E. Ciesielski, and J. A. Cotturone, 2001: Multiscale Variability of the Atmospheric Mixed Layer over the Western Pacific Warm Pool. J. Atmos. Sci., 58, 2729-2750.

Kubota, H., A. Numaguti, and S. Emori, 2004: Numerical Experiments Examining the Mechanism of Diurnal Variation of Tropical Convection. J. Meteor. Soc. Japan, 82, 1245-1260.

Liu, C. and M. W. Moncrieff, 1998: A Numerical Study of the Diurnal Cycle of Tropical Oceanic Convection. J. Atmos. Sci., 55, 2329-2344.

Louis, J.-F., 1979: A parametric model of vertical eddy fluxes in the atmosphere. Boundary-Layer Meteorology, 17, 187-202.

Mellor, G. L. and T. Yamada, 1974: A Hierarchy of Turbulence Closure Models for

Planetary Boundary Layers. J. Atmos. Sci., 31, 1791-1806.
Nakajima, T., M. Tsukamoto, Y. Tsushima, A. Numaguti, and T. Kimura, 2000: Modeling of the Radiative Process in an Atmospheric General Circulation Model. Appl. Opt., 39, 4869-4878.
Nasuno, T., H. Tomita, S. Iga, H. Miura, and M. Satoh, 2007: Multiscale Organization of Convection Simulated with Explicit Cloud Processes on an Aquaplanet. J. Atmos. Sci., 64, 1902-1921.
Neale, R. B. and B. J. Hoskins, 2000: A standard test for AGCMs including their physical parametrizations: I: the proposal. Atmospheric Science Letters, 1, 101-107.
Satoh, M., T. Matsuno, H. Tomita, H. Miura, T. Nasuno, and S. Iga, 2008: Nonhydrostatic Icosahedral Atmospheric Model (NICAM) for global cloud-resolving simulations. J. Comput. Phys., the special issue on Predicting Weather, Climate, and Extreme events, 227, 3486-3514, doi:10.1016/j.jcp.2007.02.006.
Sui, C. H., K. M. Lau, Y. N. Takayabu, and D. A. Short, 1997: Diurnal Variations in Tropical Oceanic Cumulus Convection during TOGA COARE. J. Atmos. Sci., 54, 639-655.
Sui, C. H., X. Li, and K. M. Lau, 1998: Radiative-Convective Processes in Simulated Diurnal Variations ofTropical Oceanic Convection. J. Atmos. Sci., 55, 2345-2357.
Tomita, H. and M. Satoh, 2004: A new dynamical framework of nonhydrostatic global model using the icosahedral grid. Fluid Dyn. Res., 34, 357-400.
Tomita, H., H. Miura, S. Iga, T. Nasuno, and M. Satoh, 2005: A global cloud-resolving simulation: Preliminary results from an aqua planet

experiment. Geophys. Res. Lett., 32, L08805, 10.1029/2005GL022459.

Woolnough, S.J., J.M. Slingo, and B.J. Hoskins, 2004: The Diurnal Cycle of Convection and Atmospheric Tides in an Aquaplanet GCM. J. Atmos. Sci., 61, 2559–2573.

Yasunaga, K., M. Fujita, T. Ushiyama, K. Yoneyama, Y. N. Takayabu, and M. Yoshizaki, 2008: Diurnal Variations in Precipitable Water Observed by Shipborne GPS over the Tropical Indian Ocean. SOLA, 4, 97-100, 10.2151/sola.2008-025.

Figure Captions

Fig. 1: Diurnal variations in precipitation rate averaged over the region 3°S–3°N for (a) Exp-3.5-km, and (b) Exp-7km for periods of 10 and 30 days, respectively (modified from Tomita et al. 2005). Solid and dashed lines in the panels are diurnal and semidiurnal component, respectively. The minimum value is subtracted from the data to emphasize the diurnal cycle.

Fig. 2: Longitude–time (UTC) cross-section of precipitation anomalies over the region 3°S–3°N for (a) Exp-3.5km, and (b) Exp-7km for periods of 10 and 30 days, respectively. The 12-hour running mean (from –6 to 6 hours) is subtracted from each point to obtain the anomalies. Thin solid and dashed lines indicate 1200 and 0000 LT at each longitude, respectively.

Fig. 3: Diurnal variations in column-integrated cloud water and rain (left panels), and cloud ice and snow (right panels) averaged over the region 3°S–3°N for Exp-3.5km (upper panels), and Exp-7km (lower panels) for periods of 10 and 30 days, respectively. The minimum value is subtracted from the data in each panel to emphasize the diurnal cycle.

Fig. 4: Diurnal variations in precipitable water averaged over the region 3°S–3°N for (a) Exp-3.5km, and (b) Exp-7km for periods of 10 and 30 days, respectively. The minimum value is subtracted from the data in each panel to emphasize the diurnal cycle.

Fig. 5: Time (local time)–height cross-sections of horizontal divergence averaged over the region 3°S–3°N for Exp-7km. The daily mean value is subtracted at each altitude to emphasize the diurnal cycle.

Fig. 6: Diurnal variations in (a) CAPE, (b) CIN, (c) equivalent potential temperature at the surface, and (d) height difference between LFC and LCL for

Exp-7km. The minimum value is subtracted from the data in each panel to emphasize the diurnal cycle.

Fig. 7: As for Fig. 4, but for temperature at 2 m (bar). Circles indicate diurnal variations in 2-m-temperature averaged over non-precipitating grids within 3°S–3°N.

Fig. 8: (a) Time (local time)–height cross-sections of temperature averaged over the region 3°S–3°N for Exp-7km. The daily mean value is subtracted at each altitude to emphasize the diurnal cycle. Panels (b) and (c) show diurnal and semidiurnal components of the temperature variations, respectively. In the panels, contour interval is 0.08 (K).

Fig. 9: Diurnal variations in fraction of the precipitating grid (left panels) and precipitation rate per precipitating grid (right panels) averaged over the region 3°S–3°N for Exp-3.5km (upper panels), and Exp-7km (lower panels) for periods of 10 and 30 days, respectively. The minimum value is subtracted from the data in each panel to emphasize the diurnal cycle.

Fig.10: Longitude–time (UTC) cross-section of temperature anomalies (shaded) and surface pressure anomalies (contoured) over the region 3°S–3°N for (a) Exp-3.5km, and (b) Exp-7km for periods of 10 and 30 days, respectively. The 12-hour running mean (from –6 to 6 hours) is subtracted from each point to obtain the anomalies. Thick solid and dashed lines indicate 1200 and 0000 LT at each longitude, respectively.

Fig.11: Longitude–time (UTC) cross-section of precipitable water anomalies over the region 3°S–3°N for (a) Exp-3.5km, and (b) Exp-7km for periods of 10 and 30 days, respectively. The 12-hour running mean (from –6 to 6 hours) is subtracted from each point to obtain the anomalies. Thick solid and dashed lines indicate

1200 and 0000 LT at each longitude, respectively.

Fig. 12: As for Fig. 8, but for the diabatic heating rate associated with cloud microphysics.

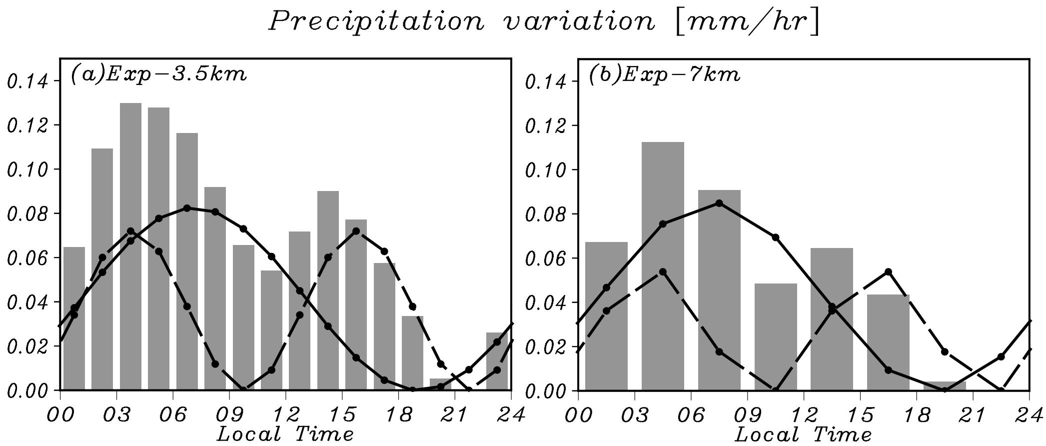

Fig. 1: Diurnal variations in precipitation rate averaged over the region 3°S–3°N for (a) Exp-3.5-km, and (b) Exp-7km for periods of 10 and 30 days, respectively (modified from Tomita et al. 2005). Solid and dashed lines in the panels are diurnal and semidiurnal component, respectively. The minimum value is subtracted from the data to emphasize the diurnal cycle.

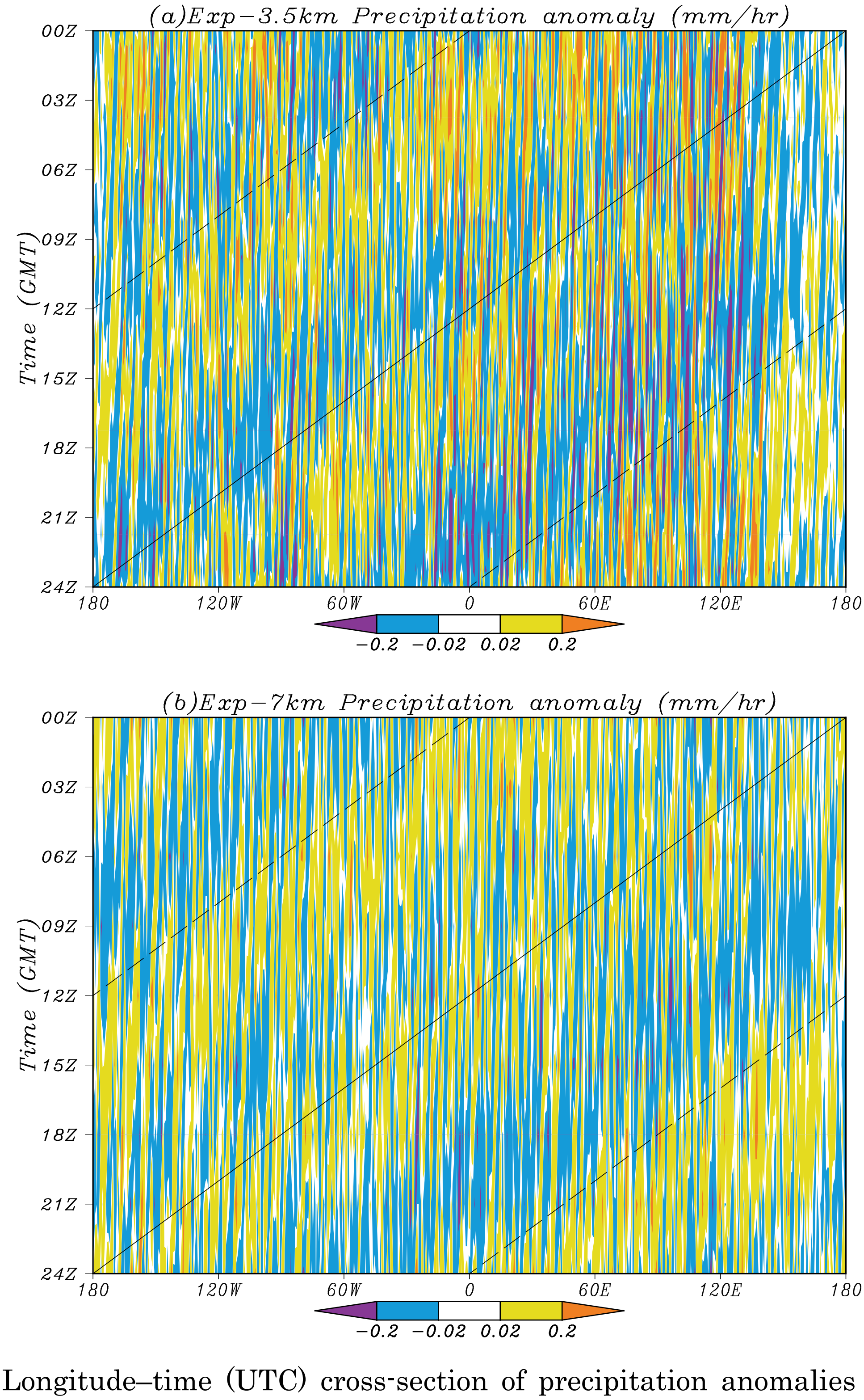

Fig. 2: Longitude–time (UTC) cross-section of precipitation anomalies over the region 3°S–3°N for (a) Exp-3.5km, and (b) Exp-7km for periods of 10 and 30 days, respectively. The 12-hour running mean (from –6 to 6 hours) is subtracted from each point to obtain the anomalies. Thin solid and dashed lines indicate 1200 and 0000 LT at each longitude, respectively.

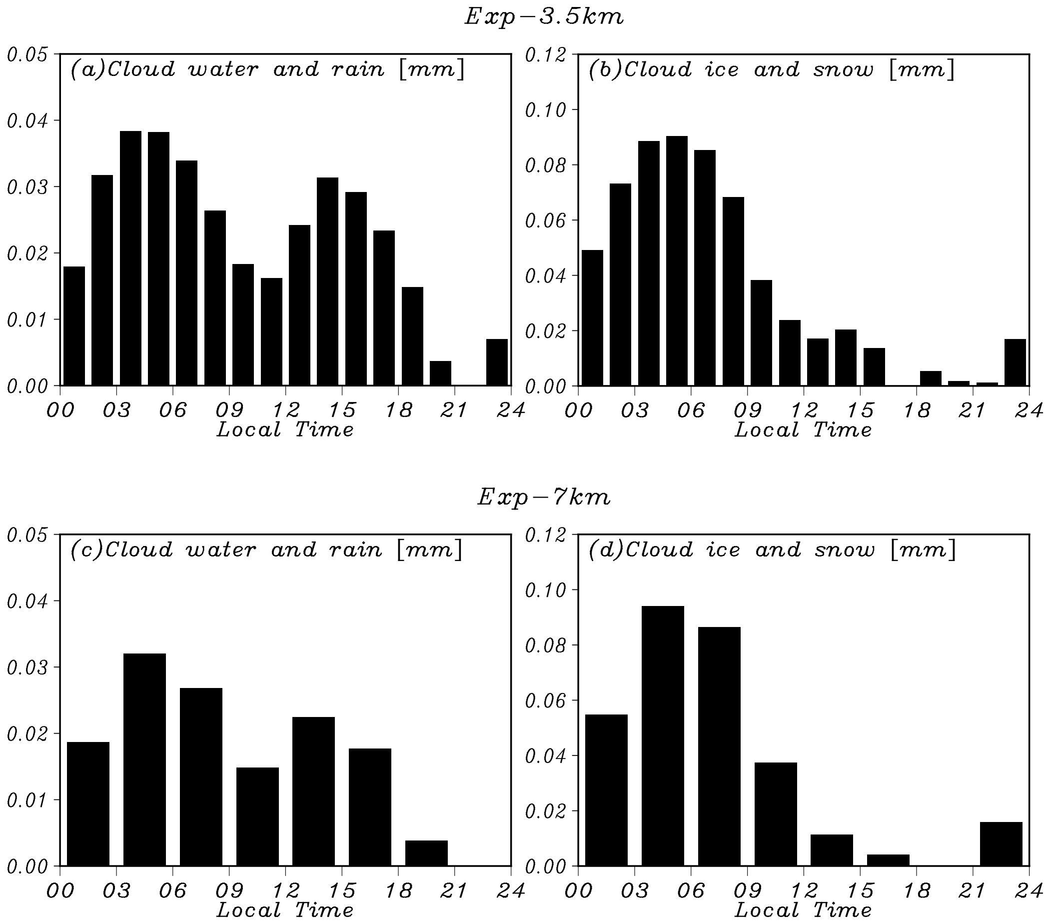

Fig. 3: Diurnal variations in column-integrated cloud water and rain (left panels), and cloud ice and snow (right panels) averaged over the region 3°S–3°N for Exp-3.5km (upper panels), and Exp-7km (lower panels) for periods of 10 and 30 days, respectively. The minimum value is subtracted from the data in each panel to emphasize the diurnal cycle.

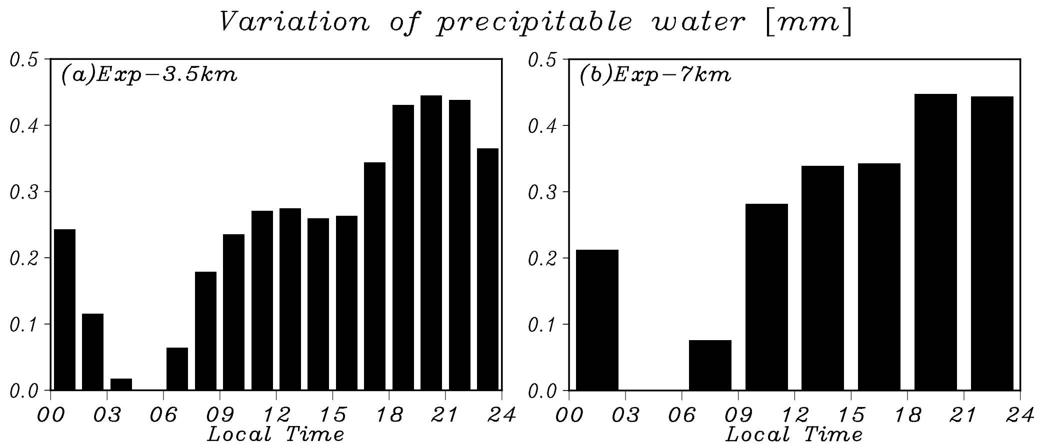

Fig. 4: Diurnal variations in precipitable water averaged over the region 3°S–3°N for (a) Exp-3.5km, and (b) Exp-7km for periods of 10 and 30 days, respectively. The minimum value is subtracted from the data in each panel to emphasize the diurnal cycle.

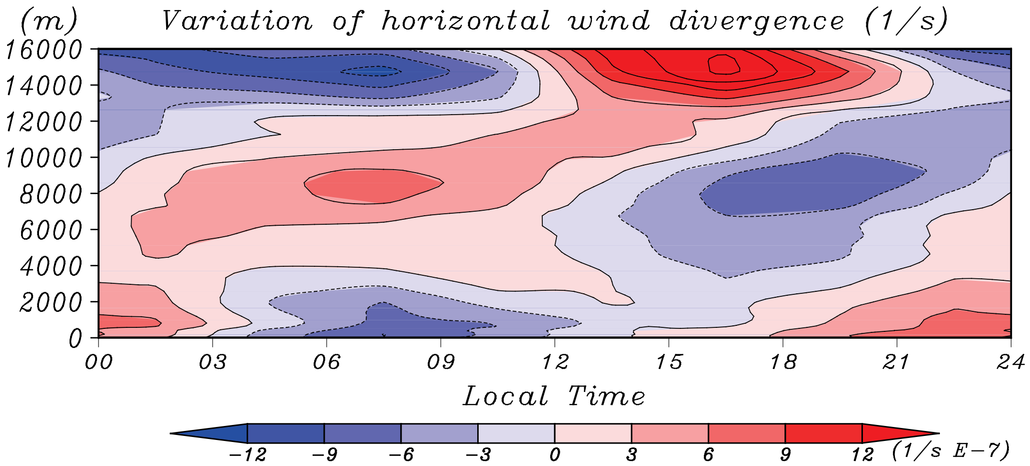

Fig. 5: Time (local time)–height cross-sections of horizontal divergence averaged over the region 3°S–3°N for Exp-7km. The daily mean value is subtracted at each altitude to emphasize the diurnal cycle.

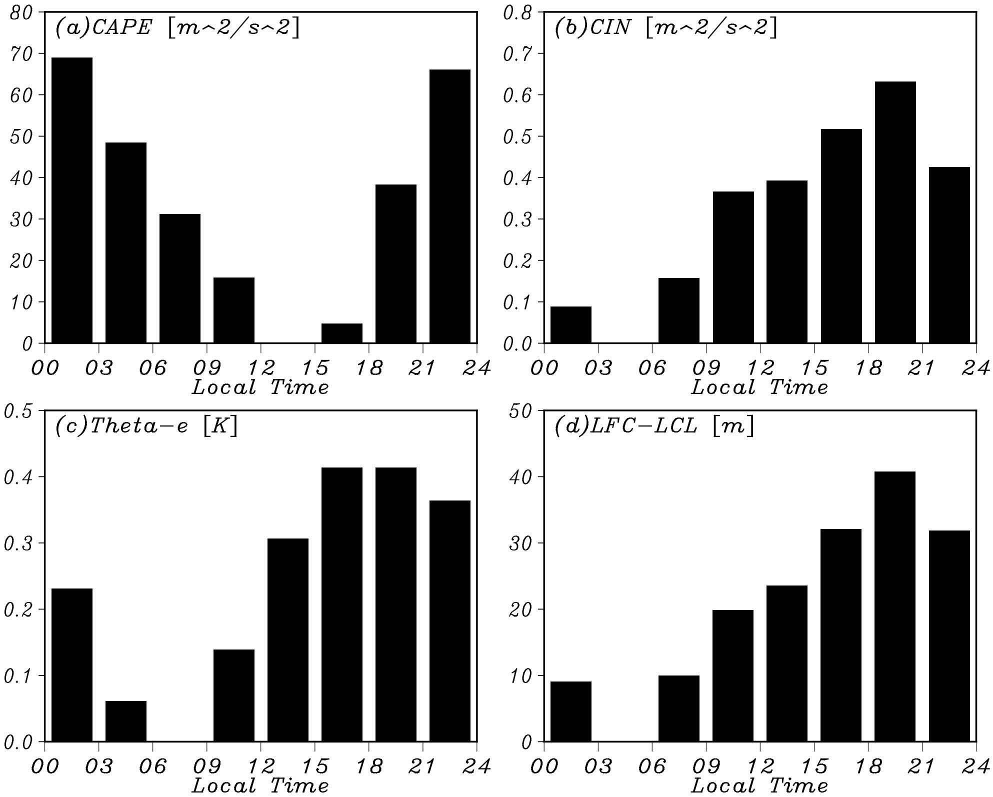

Fig. 6: Diurnal variations in (a) CAPE, (b) CIN, (c) equivalent potential temperature at the surface, and (d) height difference between LFC and LCL for Exp-7km. The minimum value is subtracted from the data in each panel to emphasize the diurnal cycle.

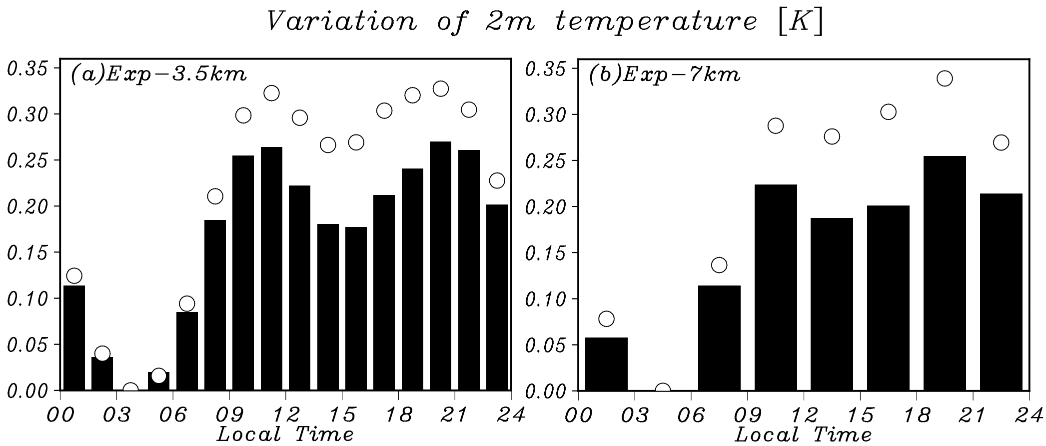

Fig. 7: As for Fig. 4, but for temperature at 2 m (bar). Circles indicate diurnal variations in 2-m-temperature averaged over non-precipitating grids within 3°S–3°N.

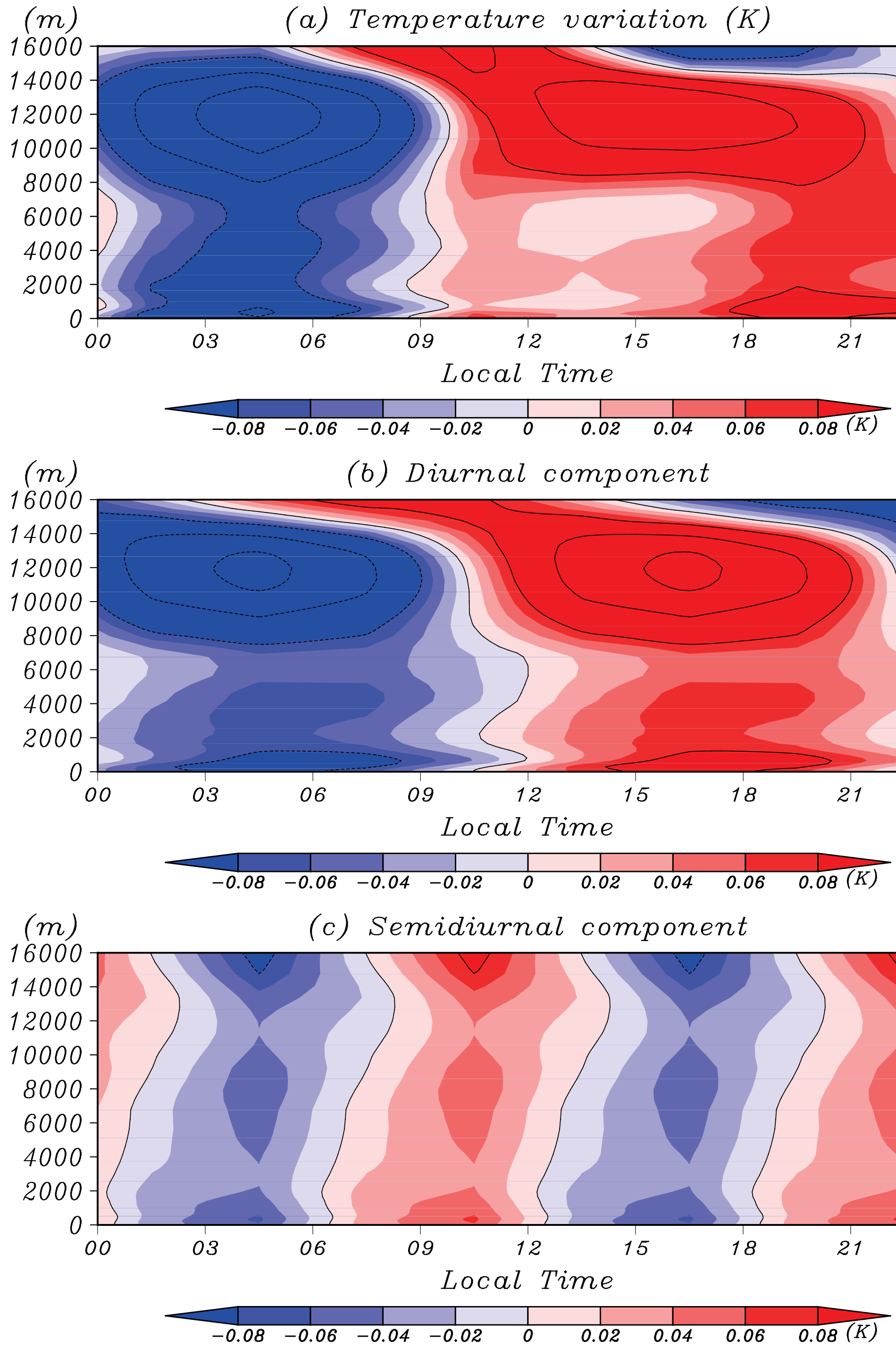

Fig. 8: (a) Time (local time)–height cross-sections of temperature averaged over the region 3°S–3°N for Exp-7km. The daily mean value is subtracted at each altitude to emphasize the diurnal cycle. Panels (b) and (c) show diurnal and semidiurnal components of the temperature variations, respectively. In the panels, contour interval is 0.08 (K).

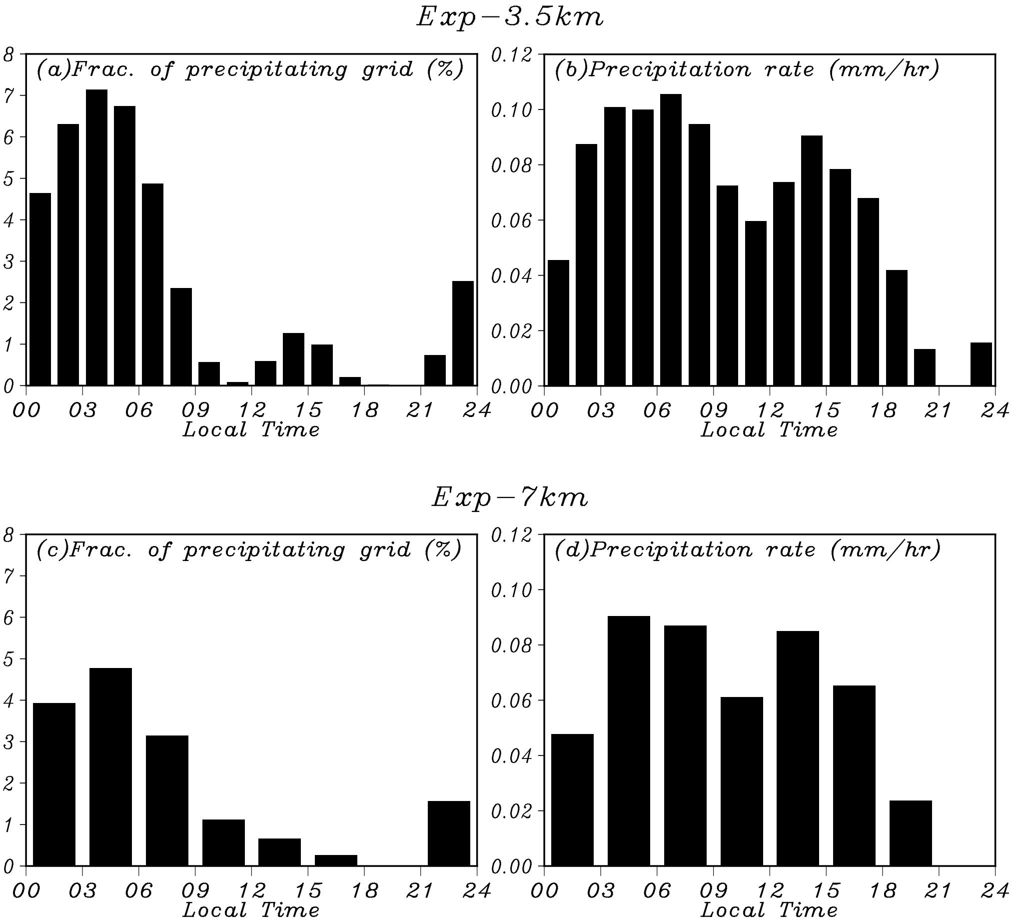

Fig. 9: Diurnal variations in fraction of the precipitating grid (left panels) and precipitation rate per precipitating grid (right panels) averaged over the region 3°S–3°N for Exp-3.5km (upper panels), and Exp-7km (lower panels) for periods of 10 and 30 days, respectively. The minimum value is subtracted from the data in each panel to emphasize the diurnal cycle.

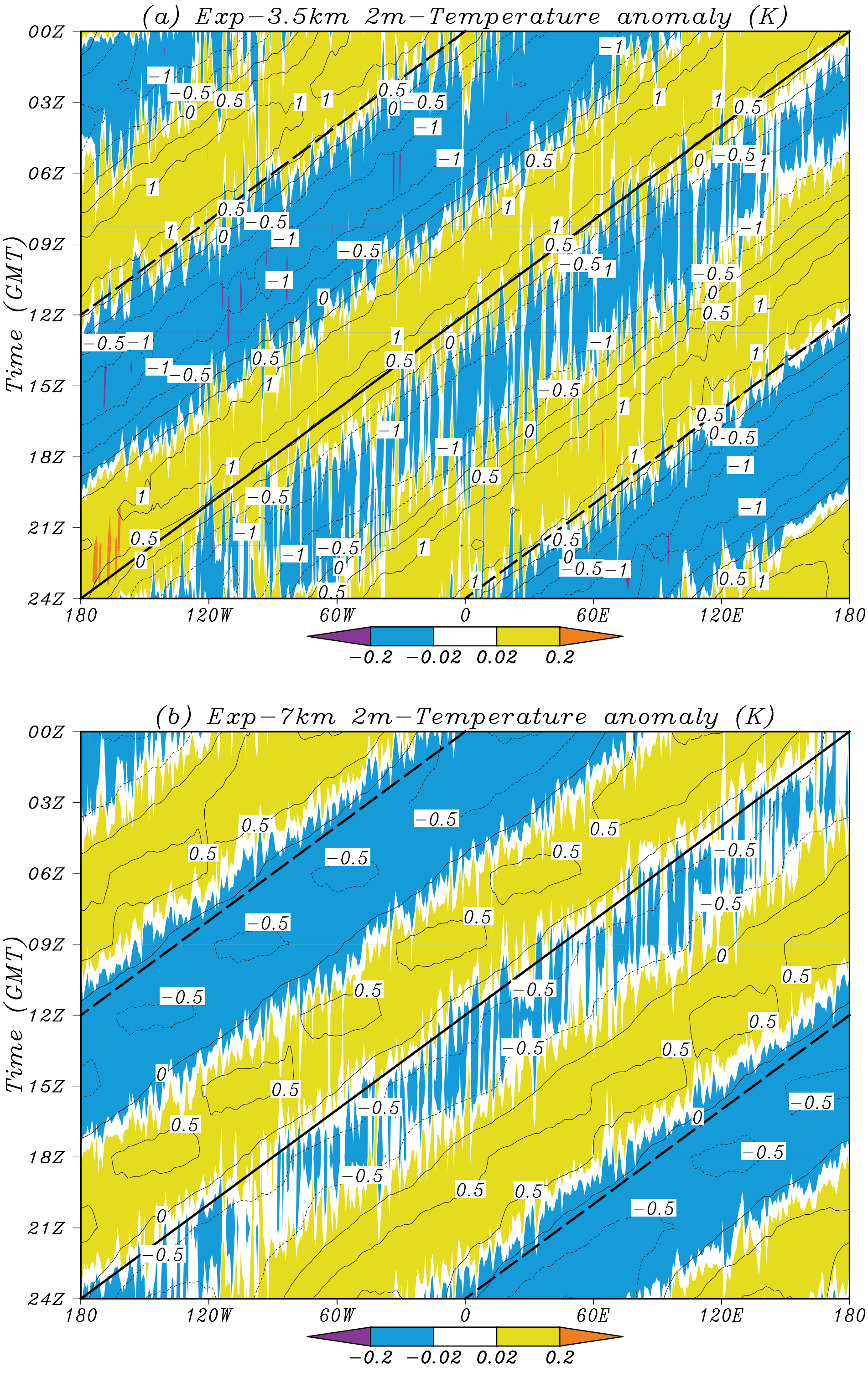

Fig.10: Longitude–time (UTC) cross-section of temperature anomalies (shaded) and surface pressure anomalies (contoured) over the region 3°S–3°N for (a) Exp-3.5km, and (b) Exp-7km for periods of 10 and 30 days, respectively. The 12-hour running mean (from –6 to 6 hours) is subtracted from each point to obtain the anomalies. Thick solid and dashed lines indicate 1200 and 0000 LT at each longitude, respectively.

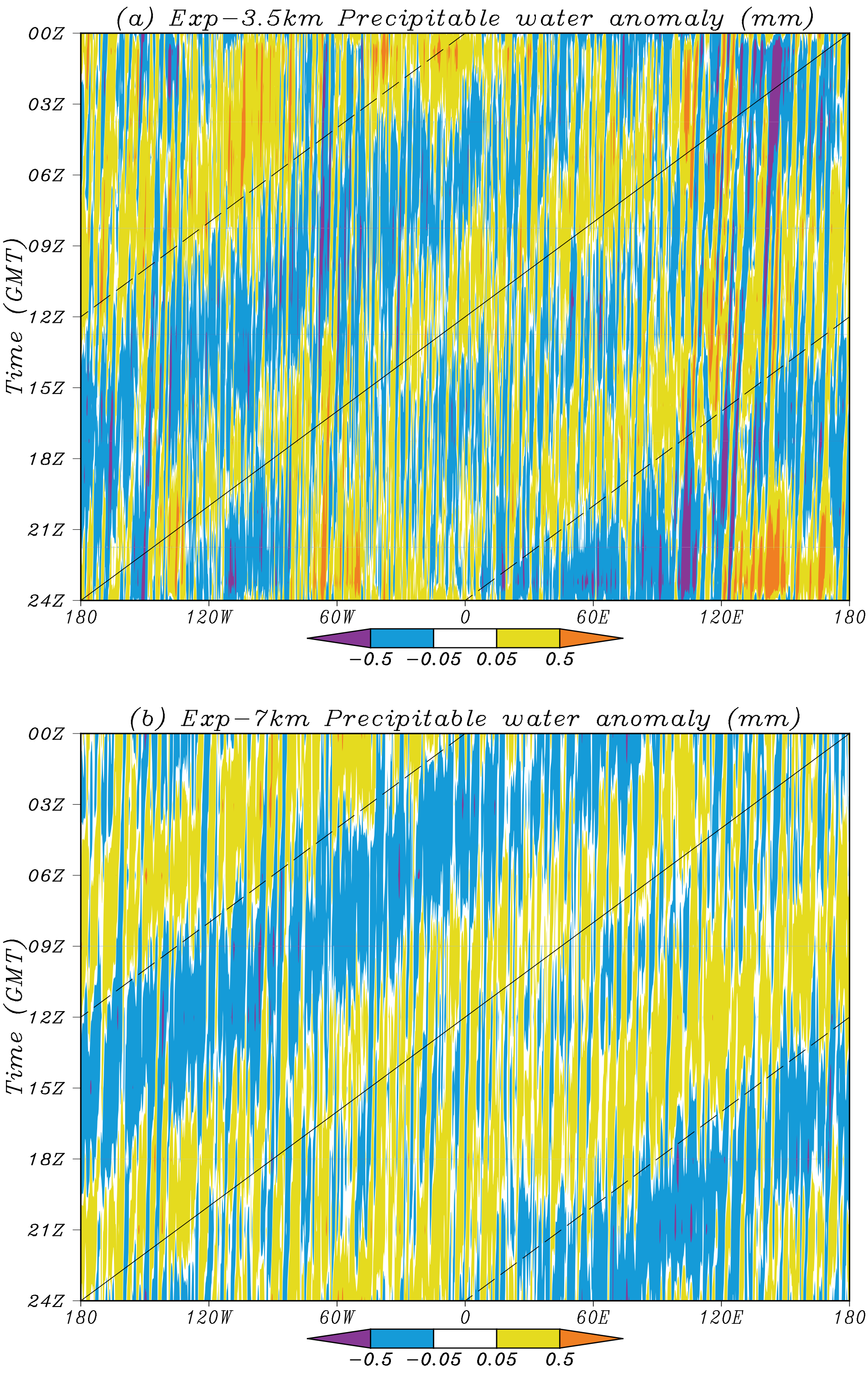

Fig.11: Longitude–time (UTC) cross-section of precipitable water anomalies over the region 3°S–3°N for (a) Exp-3.5km, and (b) Exp-7km for periods of 10 and 30 days, respectively. The 12-hour running mean (from –6 to 6 hours) is subtracted from each point to obtain the anomalies. Thick solid and dashed lines indicate 1200 and 0000 LT at each longitude, respectively.

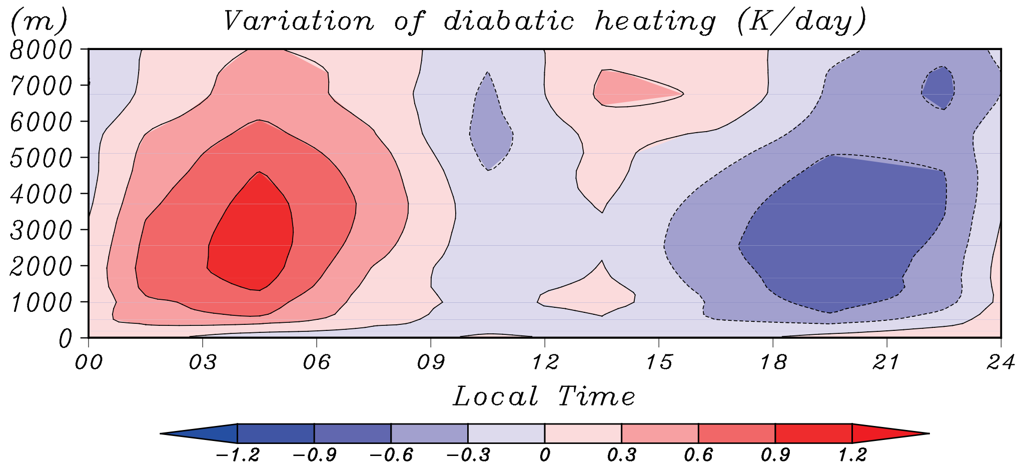

Fig. 12: As for Fig. 8, but for the diabatic heating rate associated with cloud microphysics.